

F. Zhao · B. G. M. van Wachem

Direct numerical simulation of ellipsoidal particles in turbulent channel flow

Received: 23 October 2012 / Revised: 25 February 2013 / Published online: 4 August 2013
© Springer-Verlag Wien 2013

Abstract This paper investigates the behaviour of elongated, axi-symmetric ellipsoidal particles, their interaction with turbulence, and the effects of the ellipsoids on turbulence in a turbulent channel flow with $Re_\tau = 150$. The simulations are carried out with full four-way coupling using the point-source approach: the particles are affected by the fluid, the particles affect the fluid, and the particles can collide with each other or the wall using a realistic collision algorithm. The trajectories of the ellipsoids are tracked by solving the translational and rotational equations of motion in a Quaternion framework and are closed with hydrodynamic drag and torque laws. To specifically identify the effect of particle shape, simulations of single phase channel flow are compared to simulations with spherical particles and to simulations with ellipsoids. In all cases, the driving pressure drop, to establish a flow with $Re_\tau = 150$, is kept constant. Both the spherical particles and the ellipsoidal particles have a Stokes number of 5. Although the volume fraction is very low, 0.00725 and 0.0219 % for the spheres and ellipsoids, respectively, there is some effect of the particles and the ellipsoids on the turbulence. Although the transport terms in the turbulent kinetic energy equation of the fluid are hardly affected, the turbulence kinetic energy itself decreases by 6.0 % for the flow laden with spherical particles and 4.8 % for the ellipsoidal particles. The homogeneous dissipation of turbulence kinetic energy by the fluid decreases due to the addition of particles, and the production also decreases. The particles dissipate turbulence kinetic energy of the fluid phase, predominantly in the near-wall region. Because there is a high average slip velocity in the stream-wise direction between the particles and the fluid in the near-wall region, the root mean square of the particle velocity is higher than that of the fluid velocity in this direction. In the other directions, the root mean square velocities of the particles are significantly lower than of the fluid. There is, however, a positive slip velocity between the particles and the fluid in the wall-normal direction, indicating that the particles move towards the wall with a higher momentum than that they return to the centre of the channel with. As a result, there is a 4–5 times higher concentration of particles near the wall than in the centre of the channel. As both the spherical and the ellipsoidal particles are very small, there is no major difference in their overall behaviour. However, in the near-wall region, there are some profound differences. The collision mechanism of ellipsoids with the walls is significantly different compared to spheres, the former predominantly inducing rotation resulting from a collision and the latter predominantly moving away from the wall after colliding. This is confirmed by the strong rotation as well as large root mean square of rotation of the ellipsoidal particles in the near-wall region. This results in a slight inward shift of the peak of the root mean square velocities of the fluid and the ellipsoidal particles as well as the peak in slip velocity, driving the momentum transfer, compared to the simulations with the spheres. Finally, the statistics of the orientation show that the ellipsoids align in the stream-wise direction

F. Zhao · B. G. M. van Wachem (✉)
Division of Thermofluids, Department of Mechanical Engineering,
Imperial College London, Exhibition Road,
London SW7 2AZ, UK
E-mail: Berend.van.Wachem@gmail.com
Tel.: +44-20-75947030
Fax: +44-20-75945702

in the near-wall region, because of the fluid boundary layer as well as the particle–wall collisions, but that there is no significant orientation of the ellipsoids outside of the near-wall region.

1 Introduction

Solid particles suspended in turbulent flows occur widely in industrial processes, such as the paper industry, chemical and process industry, fuel combustion processes, as well as in nature, such as sand storms and the spread of soot particles, to name a few. As such flows occur frequently, it is very important to understand the complex phenomena concerning the interaction of particles, the role of particle shape, and turbulence. In the literature, there are a large number of experimental and computational studies related to spherical particles suspended in wall-bounded turbulent flows, e.g. [9, 18–20, 22, 24, 28, 30, 32]. Assuming that particles are spheres greatly simplifies the challenge of understanding their behaviour in a turbulent flow; however, this is not often the case in reality, as the shape of solid particles in turbulence can be arbitrary in most natural and industrial processes. The behaviour of anisotropic non-spherical particles in turbulence is still poorly understood, especially the two-way and four-way coupling effects. The coupling mechanisms between the fluid phase and the non-spherical particles as well as the interactions of non-spherical particles with each other or the wall (i.e. collisions) are much more complicated than the coupling between fluid and spheres. Unlike spheres, the orientation and rotational motion of non-spherical particles can dramatically influence the hydrodynamic drag force and torque. Moreover, collisions can have a strong effect on the rotation and translation of the non-spherical particles.

An analytical equation expressing the torque on an ellipsoid in a flow under Stokes conditions has been put forward by Jeffery [17]. Subsequently, Brenner [4–6] have derived equations describing the drag and lift forces acting on various ellipsoidal particles in a flow under Stokes conditions. A further discussion of these equations is presented in Gallily and Cohen [15]. In the past few decades, only a limited number of experiments and modelling studies are reported for ellipsoidal or fibre-like particles in wall-bounded turbulent flows. Numerical studies of dispersed elongated ellipsoidal particles in wall-bounded turbulent flows are described by Fan and Ahmadi [12, 13], and Brownian effects of the fluid on the particles are discussed in [14]. A direct numerical simulation (DNS) study on the behaviour of ellipsoids is reported by Zhang et al. [37], followed by a one-way coupled DNS study performed by Mortensen et al. [26, 27] and Marchioli et al. [21]. All these studies concern one-way coupling, i.e. the particles are affected by the fluid, but the effects of the particles on the fluid as well as particle–particle interactions are neglected. In all of the above papers, the effects of the elongated shape, aspect ratio, and inertia (Stokes number) on the dispersion of elongated particles in turbulent flows have been reported and discussed, and the statistics of ellipsoidal particles are provided. Ellipsoidal particles, like spheres, accumulate in the near-wall region and preferentially concentrate in low-speed fluid regions near the wall, commonly referred to as low-speed “streaks”. Furthermore, the orientation statistics of ellipsoidal particles with different inertia and aspect ratio were investigated by Mortensen et al. [27] and Marchioli et al. [21]. It is generally found that ellipsoidal particles have a preferential orientation in the stream-wise direction in the near-wall region and that this preferential orientation increases with the aspect ratio of the particles. In the centre of the channel, the small ellipsoids are more randomly orientated.

To investigate particle effects on the fluid, two-way or four-way coupling methods are required, but the equations expressing the coupling mechanisms between the particle translation and rotation with the fluid are very complex. Recently, Andersson et al. [2] have proposed a novel torque-coupling scheme, for the two-way coupling between Lagrangian point particles and Eulerian fluid phase. Furthermore, the effects of particle–particle interactions are complex and may have a very significant effect on the rotation as well as the preferred location of the particles. Hence, even in very dilute flow, it is unclear if one-way coupling is justified: the justification of this approximation is less clear than with spherical particles.

In this study, full four-way coupling is applied in the prediction of the behaviour of ellipsoidal particles in fully developed turbulent channel flow. This implies including the effects of the fluid on the particles, the effects of the particles on the fluid, as well as realistically resolving the effect of particle–particle collisions. For the fluid phase, the particles are treated as point-sources, thus including the effects of the particles as additional source terms in the fluid phase equations. This requires the particles to be smaller than the Kolmogorov micro-scale, η_k , for this approximation to be justified [10].

In the present work, the behaviour of small anisotropic ellipsoidal particles with an aspect ratio of 3 and a Stokes number of 5 is elucidated in turbulent channel flow and compared to simulations of the channel without particles (i.e. single phase) and with spherical particles. The equations of motion of the particles are

solved in the Lagrangian framework, computing the trajectory of each individual particle by solving Newton's second law. In the previous studies mentioned above, the orientation of the particles is usually determined by unit Quaternions, or Euler parameters [3] in conjunction with the corresponding rotation matrix, to explicitly transform variables into different co-ordinate systems. The present work uses exclusively unit Quaternions, without the necessity of determining the rotation matrix. This requires a new expression of coupling the different co-ordinate systems with the unit Quaternion directly. Moreover, to determine the temporal behaviour of the unit Quaternions, a new method to integrate unit Quaternions is put forward in this paper. This new method only employs unit Quaternion multiplication, avoiding the use of addition or subtraction of Quaternions, which gives rise to inevitable numerical errors. This novel algorithm is based on a predictor–corrector method, avoiding the mixing of variables at different time levels. By the application of new rotation and collision models as put forward in this paper, more accurate particle statistics (orientation and angular velocity) can be predicted.

This paper does not only report the statistics for the particulate phase, but also the statistics for the fluid phase, the statistics for fluid–particle interactions, and the statistics of fluid dissipation, particle dissipation, and production terms in the equations governing the fluid–particle flow. Through the analysis of the turbulence kinetic energy equation of the fluid including the particles, the effects of the particles on the flow turbulence can be investigated and discussed.

The aim of this work is to investigate the behaviour of ellipsoidal particles in turbulent channel flow, by comparing with a channel flow without particles and a channel flow with spherical particles. The outline of the paper is as follows: Sect. 2 describes the governing equations of simulations and coupling mechanisms between fluid and particle phases, and new Quaternion models are derived to determine the rotation and orientation of ellipsoidal particles. An accurate collision model is introduced, and the turbulence kinetic energy (TKE) equations are also included in Sect. 2. The simulation set-up and boundary and initial conditions are discussed in Sect. 3. The results and discussion of the results are presented in Sect. 4. Finally, Sect. 5 summarises the paper and presents an outlook for the future.

2 Modelling framework

2.1 Fluid phase

The fluid is assumed incompressible, isothermal, and Newtonian and governed by the continuity and Navier–Stokes equations:

$$\frac{\partial u_i^f}{\partial x_i} = 0 \quad (1)$$

and

$$\frac{\partial u_i^f}{\partial t} + u_j^f \frac{\partial u_i^f}{\partial x_j} = -\frac{1}{\rho^f} \frac{\partial p}{\partial x_i} + \nu^f \frac{\partial^2 u_i^f}{\partial x_j^2} + \delta P_i + \Pi_i \quad (2)$$

where u_i^f is the velocity, the superscript f represents the fluid phase, and subscript i is the i th ($i = 1, 2$ or 3) component. On the right-hand side of Eq. 2, p represents pressure, and the mean constant pressure drop δP_i drives the flow. The last term Π_i in the equation describes the momentum exchange between particle and fluid phases and will be discussed in the next Section. The properties of fluid in the channel are shown in the Table 1.

In fully developed channel flow, the averaged stress in the direction of the flow is given by

$$\tau(y) = \rho^f \nu^f \frac{d\bar{u}_1}{dx_2} - \rho^f \overline{u_1^{f'} u_2^{f'}} = \tau_0 = \text{const} \quad (3)$$

Table 1 The properties of the fluid phase

Friction velocity (u_τ)	Density (ρ^f)	Kinematic viscosity (ν^f)	Friction Reynolds number (Re_τ)
0.11775 m/s	1.3 kg/m ³	1.57×10^{-5} m ² /s	150

as the Reynolds' stresses $\overline{u_1^{f'} u_2^{f'}} \rightarrow 0$ as $y \rightarrow 0$, and hence, the viscous shear stress on the wall is expressed as τ_0 . This viscous shear stress at the wall can enter into the characteristics of the flow by the combination of

$$u_\tau = \sqrt{\frac{\tau_0}{\rho^f}} \quad (4)$$

where u_τ has the units of velocity and is therefore a natural scale of the velocity close to the wall, commonly referred to as the friction velocity. The friction Reynolds number is then defined by

$$Re_\tau = \frac{u_\tau h}{\nu^f} \quad (5)$$

where h is the half height of the channel. Also, the characteristic length scale of the flow near the wall can be determined by

$$l = \frac{\nu^f}{u_\tau} \quad (6)$$

and the corresponding time scale by

$$\tau_f = \frac{\nu^f}{u_\tau^2}. \quad (7)$$

The friction Reynolds number of the channel flow is given in Table 1. Based on the friction Reynolds number, a driving pressure drop for the channel flow, δP_1 , can be determined to exactly overcome the wall shear stress as

$$\delta P_1 = \frac{\rho^f \nu^{f^2} Re_\tau^2}{h^3}. \quad (8)$$

2.2 Lagrangian anisotropic ellipsoidal particle modelling

The motion of ellipsoidal particles can be divided into translational and rotational components. To describe both components, two Cartesian co-ordinate frameworks are adopted: body space and world space. In world space, the Cartesian co-ordinates are fixed in the origin of the initial Cartesian framework, which corresponds to the Eulerian framework of the fluid phase. In body space, the axis of the co-ordinates follows the orientation of the particle, and the x axis is aligned with the principal axis of the particle. Moreover, the origin of body space is fixed on the particle mass centre. The two co-ordinate frameworks are depicted in Fig. 1. The linear motion of particles is easily described in both world and body space, but the transformation of co-ordinate systems for the rotational motion of ellipsoidal particles requires a more complex approach.

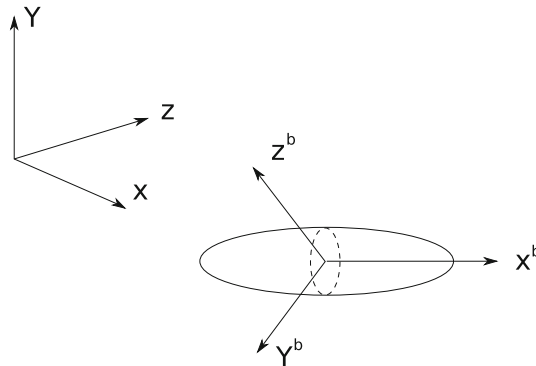


Fig. 1 The world space (*left*) and body space (on the ellipsoid) co-ordinates. The x^b axis of the body space co-ordinate system always aligns with the major axis of the ellipsoidal particle, whereas the world space co-ordinates remain fixed in space and time

2.2.1 Rotational motion

The orientation of small ellipsoidal particles in turbulent flow can significantly influence the hydrodynamic drag force and torque of particles; therefore, an accurate representation of the rotation operator determining the orientation of particles is very important. In most related papers [13,21,27,37], a rotation matrix is used to transform vector and tensor variables between body and world space. However, the application of a rotation matrix leads to a number of problems, such as error accumulation through successive matrix multiplications and singular matrix operations, sometimes referred to as “Gimbal lock” [11]. To avoid these potential problems, this paper uses Quaternions throughout. A Quaternion is a set of four numbers, defined as

$$q = [q_0, q_1, q_2, q_3]. \quad (9)$$

A Quaternion can represent scaling and rotation. To represent rotation only, Quaternions must preserve unit length during the computation, otherwise a scaling occurs simultaneously. The unit length property is expressed as

$$q_0^2 + q_1^2 + q_2^2 + q_3^2 = 1. \quad (10)$$

Successive rotations are obtained by Quaternion multiplication. The Quaternion multiplication operator is defined as

$$t = pq = \begin{pmatrix} p_0 & p_1 & p_2 & p_3 \\ -p_1 & p_0 & -p_3 & p_2 \\ -p_2 & p_3 & p_0 & -p_1 \\ -p_3 & -p_2 & p_1 & p_0 \end{pmatrix} \begin{pmatrix} q_0 \\ q_1 \\ q_2 \\ q_3 \end{pmatrix} \quad (11)$$

where Quaternion t is determined by multiplying Quaternion p with Quaternion q . As can be seen from Eq. (11), the multiplication of Quaternions is not commutative. A corresponding rotation matrix can be directly determined from the Quaternion numbers:

$$\mathbf{R} = \begin{pmatrix} 1 - 2(q_2^2 + q_3^2) & 2q_1q_2 - 2q_0q_3 & 2q_0q_2 + 2q_1q_3 \\ 2q_1q_2 + 2q_0q_3 & 1 - 2(q_1^2 + q_3^2) & 2q_2q_3 - 2q_0q_1 \\ 2q_1q_3 - 2q_0q_2 & 2q_0q_1 + 2q_2q_3 & 1 - 2(q_1^2 + q_2^2) \end{pmatrix}. \quad (12)$$

And this rotation matrix is commonly used to transform vector and tensor variables between two different co-ordinate frameworks. For a vector,

$$\mathbf{v}'_i = \mathbf{R}_{ij} \mathbf{v}_j \quad (13)$$

and for a tensor,

$$\mathbf{M}'_{ij} = \mathbf{R}_{ik} \mathbf{M}_{kl} \mathbf{R}_{lj} \quad (14)$$

where the vector \mathbf{v}' and tensor \mathbf{M}' represent the rotated counterparts of \mathbf{v} and \mathbf{M} , respectively. This paper avoids the use of rotation matrices all together. Hence, two alternatives to transformation equations corresponding to Eqs. (13) and (14), expressed in Quaternions are required. Equation (13), expressing the transformation of a vector by a rotation matrix, is equivalent to

$$\mathbf{v}' = q \mathbf{v} q^{-1} \quad (15)$$

where Quaternion q^{-1} is the conjugation of q , defined as $q^{-1} = [q_0, -q_1, -q_2, -q_3]$, and the Quaternion \mathbf{v} multiplying the Quaternions q and q^{-1} is considered as a Quaternion $[0, \mathbf{v}_1, \mathbf{v}_2, \mathbf{v}_3]$ in the above equation. For transforming a tensor by unit Quaternions, a more complex expression is derived below.

A second-order tensor \mathbf{M} can be treated as comprising three sequential column vectors,

$$\mathbf{M} = \left(\begin{pmatrix} M_{11} \\ M_{21} \\ M_{31} \end{pmatrix} \begin{pmatrix} M_{12} \\ M_{22} \\ M_{32} \end{pmatrix} \begin{pmatrix} M_{13} \\ M_{23} \\ M_{33} \end{pmatrix} \right) = (\mathbf{M}_1 \ \mathbf{M}_2 \ \mathbf{M}_3).$$

The term $\mathbf{R} \mathbf{M}$ on the right-hand side of Eq. (14) can be replaced by a tensor \mathbf{M}'' as

$$\mathbf{M}'' = \mathbf{R} \mathbf{M}. \quad (16)$$

Here, \mathbf{M}'' can be considered as transforming three sequential column vectors ($\mathbf{M}_1 \mathbf{M}_2 \mathbf{M}_3$) by a rotation matrix, so a corresponding unit Quaternion can replace the rotation matrix,

$$\begin{aligned}\mathbf{M}_1'' &= q \mathbf{M}_1 q^{-1}, \\ \mathbf{M}_2'' &= q \mathbf{M}_2 q^{-1}, \\ \mathbf{M}_3'' &= q \mathbf{M}_3 q^{-1}.\end{aligned}\quad (17)$$

Combining the above equations, a new expression is defined as

$$\mathbf{M}'' = q \mathbf{M} q^{-1} = \mathbf{R} \mathbf{M}. \quad (18)$$

Then, Eq. (14) becomes

$$\mathbf{M}' = \mathbf{R} \mathbf{M} \mathbf{R}^T = \mathbf{M}'' \mathbf{R}^T. \quad (19)$$

Transposing the tensor \mathbf{M}' gives

$$\mathbf{M}'^T = \mathbf{R} \mathbf{M}''^T, \quad (20)$$

so,

$$\mathbf{M}'^T = q \mathbf{M}''^T q^{-1} \quad (21)$$

where $\mathbf{M}''^T = (q \mathbf{M} q^{-1})^T$. Finally, the transformation of a second-order tensor by unit Quaternions can be expressed as

$$\mathbf{M}' = (q (q \mathbf{M} q^{-1})^T q^{-1})^T. \quad (22)$$

Applying Eqs. (15) and (22) avoids the application of a rotation matrix all together; the Quaternion can directly be used to transform a vector or tensor from world space to body space or vice versa.

In almost all papers concerning the time integration of unit Quaternions, the numerical integration procedure employs the subtraction or addition of unit Quaternions (e.g. [16,35]). In such papers, the time integration of unit Quaternions is determined by second-order Adams–Bashforth schemes, which require addition or subtraction operators between Quaternions. This gives rise to Quaternions exceeding unity; therefore, the Quaternions need to be normalised after each particle time-step:

$$q = \frac{q}{\sqrt{q_0^2 + q_1^2 + q_2^2 + q_3^2}}. \quad (23)$$

Due to this required normalisation procedure, numerical errors are inevitable; as the length of the Quaternion is altered, so is the relation between the Quaternion components and hence the rotation. To achieve an accurate rotational motion represented by unit Quaternions, a new Quaternion integration algorithm is put forward in this paper, based on a predictor–corrector method, completely avoiding the necessity for the addition or subtraction of Quaternions. The unit Quaternion at time level $n + 1$ is defined as

$$q_{n+1} = \tilde{q}_n q_n \quad (24)$$

where the unit Quaternion \tilde{q}_i ($i = 1, 2, 3 \dots n$) represents the change of orientation of a particle in time-step i and is given as

$$\tilde{q}_n = \left[\cos \frac{\|\boldsymbol{\omega}_{n+\frac{1}{2}}\| \delta t}{2}, \sin \frac{\|\boldsymbol{\omega}_{n+\frac{1}{2}}\| \delta t}{2} \frac{\boldsymbol{\omega}_{n+\frac{1}{2}}}{\|\boldsymbol{\omega}_{n+\frac{1}{2}}\|} \right] \quad (25)$$

where $\|\boldsymbol{\omega}_{n+\frac{1}{2}}\|$ is the length of the angular velocity $\boldsymbol{\omega}_{n+\frac{1}{2}}$. It should be noted that the length of Quaternion \tilde{q}_n is exactly unity. Therefore, the multiplication of the unit Quaternions as expressed in Eq. (25) returns a unit Quaternion by definition, and hence, no normalisation is required. The Quaternion \tilde{q}_n and $\boldsymbol{\omega}_{n+\frac{1}{2}}$ at mid-point

between two adjacent time-steps are determined by a predictor–corrector method. The angular momentum equation of particles is determined by (see e.g. [1])

$$\dot{\omega}^b = \left(I^b\right)^{-1} (N^b - \omega^b \times I^b \omega^b) \quad (26)$$

where I^b is the inertia tensor of a particle and N^b is the total torque acting on the particle. The superscript b in the equation denotes that the variable is evaluated in the body space. Elongated fibre-like ellipsoids with two equal semi-axis, which are usually referred to as spheroids, are used in this paper. The principal inertia tensor components of a prolate spheroid in body space are:

$$\begin{aligned} I_{xx}^b &= \frac{2ma^2}{5}, \\ I_{yy}^b = I_{zz}^b &= \frac{(1 + \lambda^2)ma^2}{5}. \end{aligned} \quad (27)$$

In the above equation, m and a are the mass and semi-minor axis of an ellipsoid, respectively, where the major axis of the ellipsoidal particles is aligned with the x axis of body space. The $\lambda = b/a$ is the aspect ratio of the ellipsoidal particles.

2.2.2 Translational motion

The translational motion of a particle is governed by Newton's second law,

$$\sum \mathbf{F} = m \frac{d\mathbf{u}_p}{dt} \quad (28)$$

where \mathbf{u}_p represents the particle velocity. The sum of all the external forces acting on the particle, $\sum \mathbf{F}$, includes the hydrodynamic forces (i.e. drag and lift) and the forces due to collisions with other particles or the wall. Both these contributions are discussed in the next Section.

2.3 Coupling between fluid and particle phases

The governing equation of Lagrangian particle motion is described by the Basset–Boussinesq–Oseen (BBO) equation [23]. Due to the large difference in density between the particles and the fluid, most of the terms in the BBO equation are negligible, and only drag, lift, and torque are considered.

2.3.1 Hydrodynamic drag force

The hydrodynamic drag force acting on an ellipsoidal particle is derived by Brenner [5] under creeping flow conditions as

$$\mathbf{F}_{\text{drag}} = \mu^f \pi a \mathbf{K} (\mathbf{u}_{f@p} - \mathbf{u}_p) \quad (29)$$

where μ^f is fluid dynamic viscosity, \mathbf{K} is the resistance tensor, depending on the orientation of the particle in the flow, and $\mathbf{u}_{f@p}$ represents the undisturbed fluid velocity at the centre of the particle. The resistance tensor \mathbf{K} in world space is given by

$$\mathbf{K} = (q(q\mathbf{K}^b q^{-1})^T q^{-1})^T \quad (30)$$

where \mathbf{K}^b is a constant tensor in body space. The off-diagonal components of it are 0, whereas the diagonal components are given by

$$\mathbf{K}_{xx}^b = \frac{8(\lambda^2 - 1)^{3/2}}{\left[(2\lambda^2 - 1) \ln(\lambda + \sqrt{\lambda^2 - 1}) - \lambda(\sqrt{\lambda^2 - 1}) \right]}, \quad (31)$$

$$\mathbf{K}_{yy}^b = \mathbf{K}_{zz}^b = \frac{16(\lambda^2 - 1)^{3/2}}{\left[(2\lambda^2 - 3) \ln(\lambda + \sqrt{\lambda^2 - 1}) + \lambda(\sqrt{\lambda^2 - 1}) \right]}. \quad (32)$$

A more detailed derivation and discussion of the resistance tensor can be found in [15].

2.3.2 Hydrodynamic torque

In Jeffery [17], the hydrodynamic torque acting on ellipsoids in a shear flow under Stokes flow condition is derived analytically. The torque components of an ellipsoid, of which the major axis is along the x^b -axis, are given in body space as

$$N_x^{b,h} = \frac{32\pi\mu^f a^3\lambda}{3(\alpha_2 + \alpha_3)}(\Omega_{zy}^b - \omega_x^b), \quad (33)$$

$$N_y^{b,h} = \frac{16\pi\mu^f a^3\lambda}{3(\alpha_3 + \lambda^2\alpha_1)} \left[(1 - \lambda^2)\mathbf{S}_{xz}^b + (1 + \lambda^2)(\Omega_{xz}^b - \omega_y^b) \right], \quad (34)$$

$$N_z^{b,h} = \frac{16\pi\mu^f a^3\lambda}{3(\alpha_2 + \lambda^2\alpha_1)} \left[(\lambda^2 - 1)\mathbf{S}_{yx}^b + (1 + \lambda^2)(\Omega_{yx}^b - \omega_z^b) \right] \quad (35)$$

where the \mathbf{S}^b and Ω^b represent the fluid strain rate tensor and the rotation tensor in body space, given as

$$\mathbf{S}_{ij}^b = \frac{1}{2} \left(\frac{\partial u_i^{fb}}{\partial x_j} + \frac{\partial u_j^{fb}}{\partial x_i} \right), \quad (36)$$

$$\Omega_{ij}^b = \frac{1}{2} \left(\frac{\partial u_i^{fb}}{\partial x_j} - \frac{\partial u_j^{fb}}{\partial x_i} \right). \quad (37)$$

It should be noted that the derivatives are to be evaluated in body space, in the framework of the particle, and not in the Eulerian framework in which the fluid equations are solved. In Eqs. (33)–(35), the constants α_1 , α_2 , and α_3 are defined by

$$\alpha_1 = -\frac{2}{\lambda^2 - 1} - \frac{\lambda}{(\lambda^2 - 1)^{3/2}} \ln \left[\frac{\lambda - (\lambda^2 - 1)^{1/2}}{\lambda + (\lambda^2 - 1)^{1/2}} \right], \quad (38)$$

$$\alpha_2 = \alpha_3 = \frac{2}{\lambda^2 - 1} + \frac{\lambda}{2(\lambda^2 - 1)^{3/2}} \ln \left[\frac{\lambda - (\lambda^2 - 1)^{1/2}}{\lambda + (\lambda^2 - 1)^{1/2}} \right]. \quad (39)$$

The total torque on the particle is the sum of the hydrodynamic torque and the torque arising from possible collisions,

$$\mathbf{N}^b = \mathbf{N}^{b,h} + \sum_{\text{collisions}} \mathbf{N}^{b,c}, \quad (40)$$

and this torque is used to compute the acceleration of angular momentum, Eq. (26). A more detailed derivation and discussion of the hydrodynamic torque on an ellipsoid in Stokes flow can be found in [15].

2.3.3 Particle effects on fluid phase

The effects of the linear momentum of the particles on the fluid are included in the fluid momentum equation, Eq. (2), as a source term. The effect of the rotational momentum of the particles on the fluid is assumed small and has been neglected. The inclusion of this source term is referred to as the “particle-source-in-cell” method. The PSI-Cell method of Crowe et al. [8] is used, and the force of the particle on the fluid in each computational cell is volume averaged and added as a source term in the momentum equation:

$$\boldsymbol{\Pi} = -\frac{1}{V_{\text{cell}}^f} \sum_{i=1}^{N_p} \mathbf{F}_{\text{drag}}^i \quad (41)$$

where the summation is for all particles and fractions of them in each computational cell. In this way, the Lagrangian particle properties are transformed to Eulerian by volume averaging. Note that this method involves the interpolation of Lagrangian quantities to the fluid cell centres. Yeung and Pope [36] perform a study on the interpolation schemes in homogeneous and isotropic turbulence and report that the cubic spline interpolation method has the least effect on the fluid energy spectrum. Therefore, cubic splines are used in this work to determine $u_f|_p$ at each of the particle positions in the drag equation (29).

2.4 Particle collision modelling

In many gas-particle flows, both particle–particle and particle–wall collisions are important mechanisms for predicting the behaviour of the flow. For ellipsoidal-shaped particles, it is not precisely clear at what mass loading collisions become important. Therefore, this paper derives and applies a realistic deterministic collision model for the particles. To achieve this, all potential collisions must be correctly detected in order to add their contribution to the overall force on each of the particles involved in the collision. Moreover, the particle–wall collisions are required to keep the particles in the domain.

Firstly, all particle–particle and particle–wall contact points must be determined. This is achieved by placing a large number of small, fictitious spheres inside each of the ellipsoids, so that the hull of the small spheres in each ellipsoid provides an accurate representation of the surface of the ellipsoid. The contact points of collision are then determined by considering the contact points between the small spheres of different but neighbouring ellipsoids, or between the small spheres and the walls of the channel. Once the contact point has been identified, the local displacement can be determined at the point of contact. It should be noted that the small spheres are only used to determine the point of contact, not to determine the actual parameters of the collision.

A small overlap, which is determined at the identified point of contact, represents the local deformation of the colliding particle. The repellent force resulting from the deformation of the contact point is determined by using a Hertzian-like force model. This soft-sphere collision model is applied to resolve particle–particle and particle–wall collisions. The overlap is used as a measure to estimate the local deformation of the particle at the point of collision and leads to normal and tangential forces based upon the work of [25],

$$\begin{aligned}\mathbf{F}_n(t) &= K_n(t)\delta_n^{\frac{3}{2}}(t)\mathbf{n}(t), \\ \mathbf{F}_t(t) &= \min(\mu\mathbf{F}_n(t), K_t(t)\delta_t(t))\end{aligned}$$

where μ is the coefficient of friction, $\delta_n(t)$ is the scalar representing the normal displacement, and $\delta_t(t)$ is the vector representing the total tangential displacement mapped onto the current reference frame. The tangential displacement vector is determined by integrating the successive tangential displacements and mapping this into the current frame of reference of the collision. K_n and K_t are the spring constants for the normal and tangential forces, respectively, as predicted by Hertzian contact theory,

$$\begin{aligned}K_{n,l}(t) &= \frac{4}{3}E^*\sqrt{r(t)}, \\ K_t(t) &= 8G^*\sqrt{r(t)\delta(t)}\end{aligned}$$

where $r(t)$ represents the local radius of the particle–particle contact and the subscript l represents loading, i.e. the particles moving towards each other. To account for the dissipative nature of the collision, a coefficient of restitution is introduced to determine the spring constant value for unloading, represented by the subscript u , following [34]

$$e = \sqrt{\frac{K_{n,u}}{K_{n,l}}}. \quad (42)$$

The subsequent forces and torques of the particle–particle and particle–wall collisions are then added to the particles in contact. The collisional torque for each collision is determined as

$$\mathbf{N}^c = (\mathbf{F}_n + \mathbf{F}_t) \times \mathbf{X}_{mp-cp} \quad (43)$$

where \mathbf{X}_{mp-cp} represents the vector from the centre of the particle to the contact point of the collision. Note that the above equation is expressed in world space and is converted to body space for application in Eq. (40). The collision algorithm can be summarised as follows:

- (i) Identify all the points of contact between particle–particle and particle–wall.
- (ii) At each point of contact, determine the normal and tangential overlaps, which represent the local deformation of the solid.
- (iii) From the overlaps, determine the resulting normal and tangential repellent forces associated with each contact point.
- (iv) From the forces, determine the resulting torque on the particle.
- (v) Apply the forces and the torque to the equations of motion of each corresponding particle.

2.5 Turbulence kinetic energy equation

To study the effect of the particles on turbulence, an analysis of the terms on the turbulence kinetic energy (TKE) equation is required. Reynolds decomposition is applied when analysing TKE equation. A variable u can be divided into two parts: a mean component and a random fluctuating component,

$$\mathbf{u} = \mathbf{U} + \mathbf{u}' \quad (44)$$

where \mathbf{U} is the mean component and \mathbf{u}' is the fluctuating part. The turbulence kinetic energy is defined as

$$k = \frac{1}{2} \langle u_i'^f u_i'^f \rangle, \quad (45)$$

and the TKE equation for single phase fully developed channel flow including the effect of particles can be simplified as

$$\frac{d}{dy} \left(\frac{1}{2} \langle u_y'^f u_i'^f u_i'^f \rangle + \frac{u'^f p'}{\rho^f} - \nu^f \frac{dk}{dy} \right) = \mathcal{P} - \tilde{\varepsilon} + \varepsilon_p \quad (46)$$

where the left-hand-side terms are commonly referred to as the transport terms of TKE and where \mathcal{P} and $\tilde{\varepsilon}$ are the production and the homogeneous dissipation, respectively, and where the particle dissipation rate ε_p is derived from the particle-source term in Eq. (2). In fully developed channel flow, the production and homogeneous dissipation rate are given by

$$\mathcal{P} = - \langle u_x'^f u_y'^f \rangle \frac{\partial U_x^f}{\partial y}, \quad (47)$$

$$\tilde{\varepsilon} = \nu^f \langle \frac{\partial u_i'^f}{\partial x_j} \frac{\partial u_i'^f}{\partial x_j} \rangle, \quad (48)$$

and the particle dissipation rate is given by the equation

$$\varepsilon_p = \langle \Pi_i' u_i'^f \rangle \quad (49)$$

The particle dissipation rate represents the attenuation of turbulence due to the presence of the particles.

The symbol $\langle \rangle$ represents the averaging operator in the above equations. The terms on the left-hand side of Eq. (46) are transport of kinetic energy in an inhomogeneous field: turbulence itself, the pressure fluctuations, and viscous stresses, respectively. Due to the homogeneity of stream-wise (x) and span-wise (z) directions, all the items of these two direction gradients are zero, and the full TKE equation can be simplified to Eq. (46), where only gradients remain which are in the y -direction.

For particle-laden turbulent channel flow, an additional term arises on the TKE equation, representing the effect of the particles. This term originates from the source term Π_i , presented on the momentum equation, Eq. (2).

2.6 Correlation between particle and fluid velocity

In the equation for the drag of the ellipsoidal particles, Eq. (29), the force is determined by the velocity difference between the particle and fluid at the position of the particle. Hence, the velocity relationship between two phases plays an important role: it determines where energy is transferred from the fluid to the particles or vice versa. The correlation coefficient of relative velocities at the particle point is defined as

$$\hat{\rho}_{fp} = \frac{\langle \mathbf{u}'_{f@p} \mathbf{u}'_p \rangle}{\left[\langle \mathbf{u}_{f@p}^2 \rangle \langle \mathbf{u}_p^2 \rangle \right]^{\frac{1}{2}}}. \quad (50)$$

For high Stokes number particles, i.e. particles with large inertia, it is expected to find a small correlation between the particle velocity and fluid velocity. However, as the particle inertia decreases, the particles tend to behave more and more as fluid particles. It is expected that the particle shape also plays an important role on the velocity correlation. As non-spherical particles may have a preferential orientation, this will affect the correlation significantly. In this work, the velocity correlation of ellipsoidal particles will be compared to spherical particles with the same Stokes number.

3 Simulation set-up

In this work, the properties of the fluid phase and the computational domain are the same as in the work of Marchioli et al. [21,22], who have studied this channel case for spherical and ellipsoidal particles. The size of the channel computational domain is $4\pi h \times 2h \times 2\pi h$ in x , y , and z directions, respectively, in which $h = 0.02$ m is the half height of the channel, and the mean flow is in the x direction. There are solid walls in the low and high y directions, and in all other directions, periodic boundaries are applied. The corresponding flow conditions are given in Table 1. This leads to a required external pressure drop based on Eq. (8), which for the flow conditions specified in Table 1 leads to $\delta P_1 = 0.90123$ Pa/m.

3.1 Computational parameters

This domain is discretised in $161 \times 171 \times 161$ grid points, where the grid spacing is uniform in the x and z directions. The grid spacing in the y direction is refined towards the walls, using a tanh distribution with a growth factor of 1.6 on both sides. This ensures 4 grid points in the first $5 y^+$ layer of the wall. The temporal operator in the Navier–Stokes equations is approximated with a 3 point backward Euler scheme with second-order accuracy with respect to the time-step. The non-dimensional time-step for the fluid phase, $\Delta t^+ = \frac{\Delta t}{\tau_f}$, is 0.08826. The advective terms in the Navier–Stokes and continuity equations are approximated with a central scheme, with second-order accuracy with respect to the local grid spacing.

3.2 Particles

This paper compares simulations of a turbulent channel flow with the same turbulent channel flow with spherical particles and the channel flow with ellipsoidal particles. The ellipsoidal particles have an aspect ratio of $\lambda = 3$. Both the spheres as well as the ellipsoids have a Stokes number of 5. The response time for the ellipsoidal particles, τ_p , is derived by Shapiro [29] as

$$\tau_p = \frac{2a^2 \frac{\rho_p}{\rho_f}}{9\nu f} \frac{\lambda \ln \left(\lambda + (\lambda^2 - 1)^{\frac{1}{2}} \right)}{(\lambda^2 - 1)^{\frac{1}{2}}}. \quad (51)$$

The properties of the particles considered in this paper are summarised in Table 2. For the translational velocity, a velocity-Verlet temporal discretisation is employed with a dimensionless time-step of $\Delta t^+ = \frac{\Delta t}{\tau_f} = 8.826 \times 10^{-5}$. The same time-step is used for the integration of the unit Quaternions. This time-step is significantly smaller than the fluid time-step, but only such a small time-step can guarantee the accuracy of the soft-sphere collision model for the given material and flow parameters.

For the simulations concerning spherical and ellipsoidal particles, 200,000 particles are randomly placed in the domain of the channel with fully developed single phase flow as initial conditions for the fluid. The initial velocity of the particles is the same as the local fluid velocity, and the rotational velocity is set to zero. The simulations are carried out in our in-house code MultiFlow [7,33].

4 Results and discussion

In this Section, the results of three different simulations are compared to each other and analysed: a turbulent channel flow, the same channel flow with spherical particles, and the same channel flow with ellipsoidal particles with the same Stokes number as the spheres. Both the fluid and particle velocity statistics are analysed, as well as the correlations between the particle and the fluid. Also, the effect of the different particles on the turbulence

Table 2 The properties of particles

Shape	Aspect ratio (λ)	Stokes number (St)	Density (ρ_p)	Semi-major axis (b)
Sphere	1.0	5	225.68 kg/m ³	47.99 μ m
Ellipsoid	3.0	5	120.77 kg/m ³	143.96 μ m

is reported, by analysing the terms on the TKE equation, and the effects are discussed. Finally, the orientation and angular velocity of the ellipsoidal particles are reported, discussed, and compared to earlier findings.

4.1 Single phase

To ensure the simulation, results for the channel flow are in accordance with previous results of [22], in which a number of researchers compare their findings on this case, and Figs. 2 and 3 compare the results of the current framework with the results of the UUD group (Marchioli and Soldati) [22] for the stream-wise velocity and the RMS of the stream-wise fluid velocity, respectively. As can be seen, the results are in very good agreement.

4.2 Particle-laden channel flow

4.2.1 Distribution of particles

In this study, the average volume fractions, $\langle \alpha \rangle$ of the spherical particles, and ellipsoidal particles are around 0.00725 and 0.0219 %, respectively. Figure 4 shows the relative volume fraction, $\frac{\alpha(y)}{\langle \alpha \rangle}$, showing a

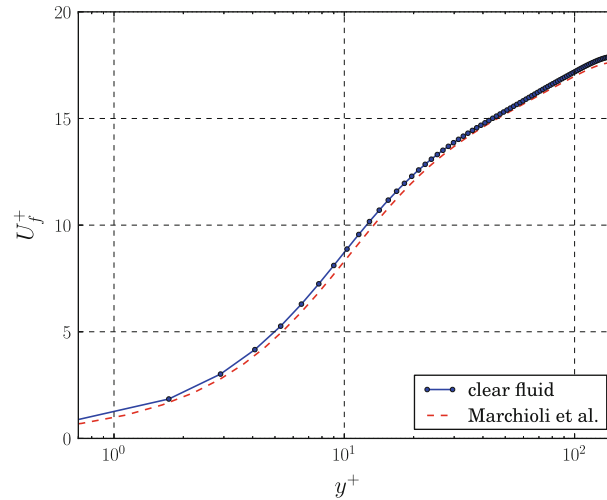


Fig. 2 Fluid stream-wise direction mean velocities as functions of the distance to the wall for: clear fluid (*solid line with circle*), Marchioli et al. [22] data (*dashed line*)

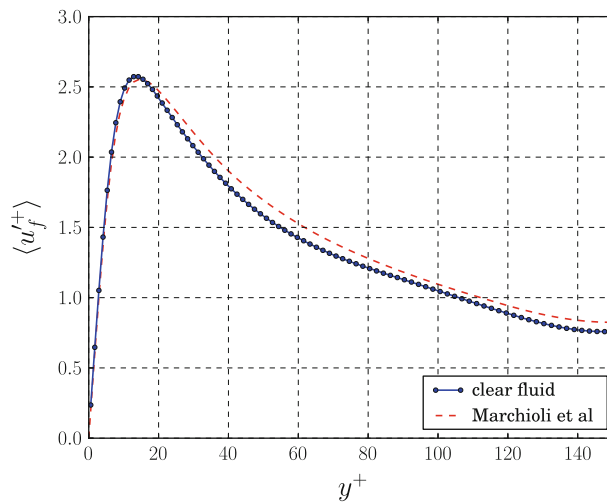


Fig. 3 Fluid stream-wise direction RMS velocities as functions of the distance to the wall for: clear fluid (*solid line with circle*), Marchioli et al. [22] data (*dashed line*)

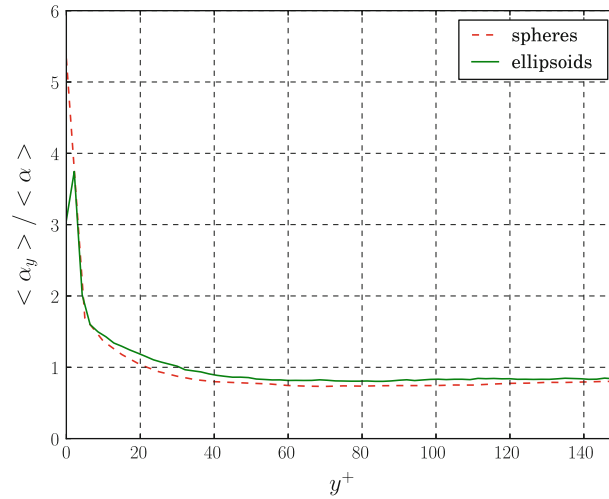


Fig. 4 Relative volume fraction as a function of distance to the wall for: spherical case (*dashed line*), ellipsoidal case (*solid line*)

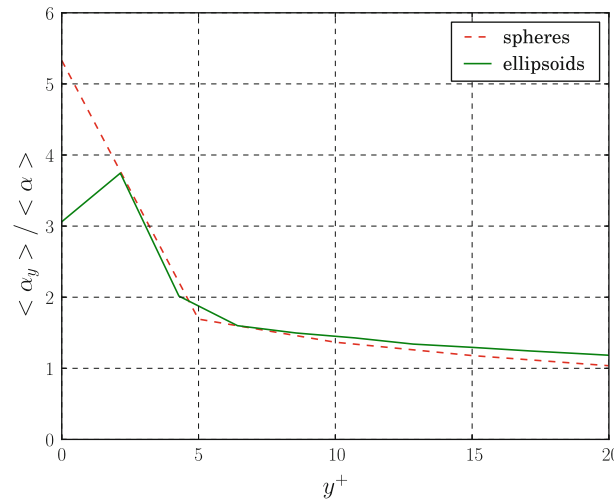


Fig. 5 Relative volume fraction in near-wall region as function of distance to the wall for: spherical case (*dashed line*), ellipsoidal case (*solid line*)

strong accumulation of the particles in the near-wall region. The difference between the spheres and the ellipsoids is small, but the relative volume fraction of the ellipsoids peaks slightly inside of the channel, due to the larger size and the different dynamics of the collisions of the ellipsoids. Figure 5 shows a close-up of the near-wall region, where it can be observed that the volume fraction of the ellipsoids reaches a maximum a bit away from the wall, at $y^+ = 2.5$. In both cases, the number of particles in the near-wall region are several times (≈ 4 – 5) larger than the number in centre region. Figure 6 shows an instantaneous fluid velocity and the distribution of ellipsoids in a wall-parallel plane $y^+ = 6.5$. It can be clearly seen that more ellipsoids accumulate in the low-speed streaks (blue region), whereas the high-speed region (red region) contains only few ellipsoids. This is in line with earlier observations of spherical particles. Figure 7 shows an instantaneous contour plot of wall-normal fluid velocity and the distribution of the ellipsoids in the X – Y plane at $z^+ = 942$. In this Figure, only a few ellipsoids appear in the relative large velocity and low strain rate zones (dark blue and red zones), but the ellipsoids preferentially concentrate in low velocity and high strain regions (yellow and green areas between the high velocity zones). The preferential concentration of particles has been previously reported by Squires and Eaton [31] for spherical particles.

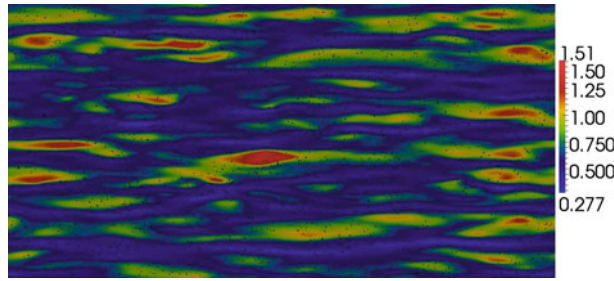


Fig. 6 Instantaneous stream-wise fluid velocity (indicated by *colour*) and distribution of the ellipsoids in the cross-sectional $X-Z$ plane at $y^+ = 6.5$ (colour figure online)

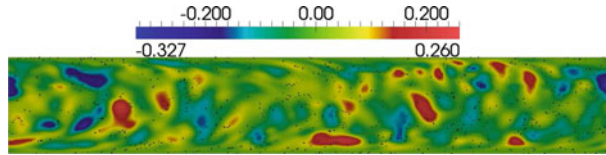


Fig. 7 Instantaneous wall-normal velocity (indicated by *colour*) and distribution of the ellipsoids in the cross-sectional $X-Y$ plane at $z^+ = 942$ (colour figure online)

4.2.2 Velocity statistics

In this Section, the velocity statistics of both phases are reported and discussed, including the mean stream-wise velocity, the root mean square (RMS) of velocity in all directions, the Reynolds stresses, and the relative velocity between fluid and particles. Although the volume fraction of the particles in both cases is very small, the presence of particles in turbulent flow still influences the fluid statistics slightly.

4.2.3 Fluid velocity statistics

Figure 8 compares the mean fluid stream-wise velocities for the 3 different cases: the clear channel, the channel with the spheres, and the channel with the ellipsoids. Under the dilute flow condition, the difference of mean stream-wise velocity between particle-fluid and clear fluid simulations is very small, but is slightly affected by the particles. The fluid velocity in the particle-laden case is generally slightly lower in the region of $2 < y^+ < 40$. In the very near-wall region as well as the centre of the channel, the fluid velocity for the spherical particle-laden case is the same as in the case of the clear channel. The mean fluid velocity is slightly

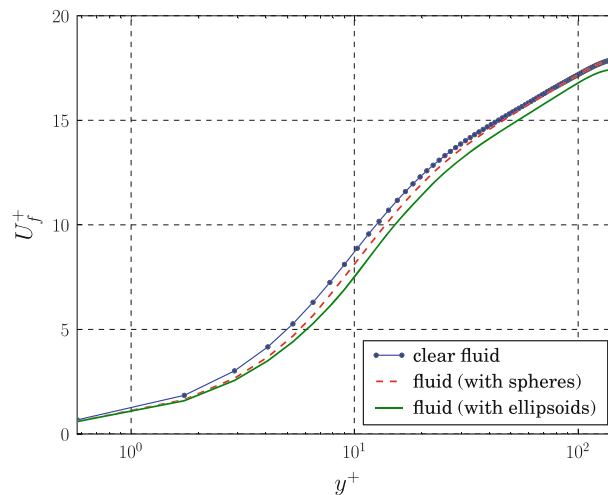


Fig. 8 Fluid stream-wise direction mean velocities as functions of distance to the wall for: single phase (*solid line with circle*), fluid with spherical particles (*dashed line*), fluid with ellipsoidal particles (*solid line*)

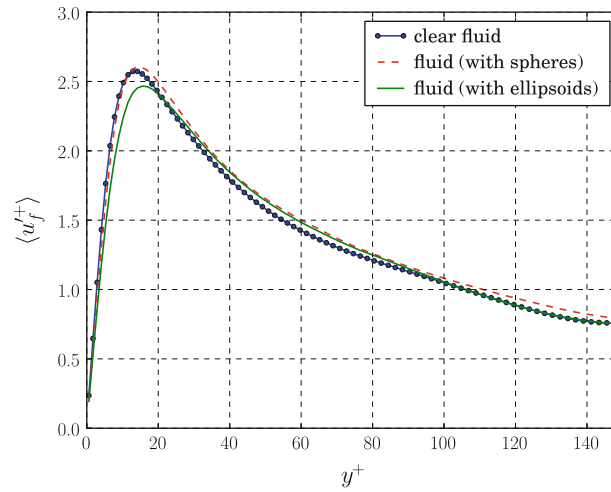


Fig. 9 Fluid stream-wise direction RMS velocities as a function of the distance to the wall for: single phase (*solid line with circle*), fluid with spherical particles (*dashed line*), fluid with ellipsoidal particles (*solid line*)

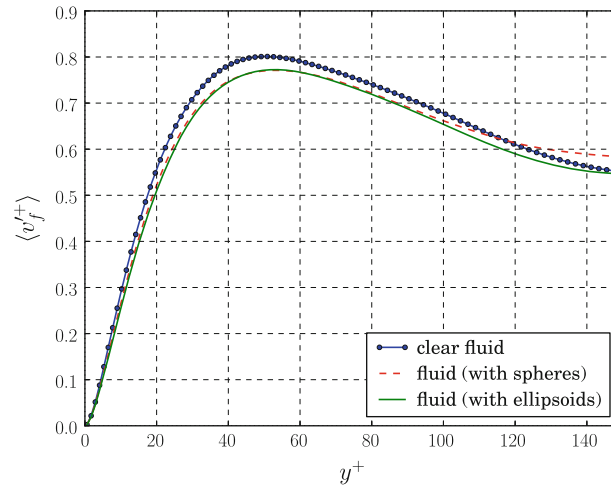


Fig. 10 Fluid wall-normal direction RMS velocities as a function of the distance to the wall for: single phase (*solid line with circle*), fluid with spherical particles (*dashed line*), fluid with ellipsoidal particles (*solid line*)

lower for the channel flow laden with ellipsoidal particles, most likely because the volume fraction in this case is slightly higher compared to the case with spheres. As the flow is driven with the same pressure drop in all 3 cases, a slightly lower fluid bulk velocity, and therefore value of Re_{bulk} , is observed for the two particle-laden cases. The bulk fluid velocity decreases from 1.803 m/s in clear channel to 1.781 m/s for the flow laden with spheres, and 1.721 m/s for the flow laden with ellipsoids. Hence, part of the driving pressure drop is used to account for the additional dissipation caused by the behaviour of the particles.

The fluid RMS velocities are shown in Figs. 9, 10 and 11 for the 3 different orthogonal directions. Again, due to the low mass loading of the particles in the flow, the results of the two cases with particles are very similar to the clear channel flow statistics. The peak values of the span-wise and wall-normal fluid RMS velocities are slightly reduced, but the fluctuations slightly increase in the stream-wise direction for the channel with spherical particles. Hence, the particles seem to stabilize the flow slightly in the span-wise and wall-normal directions, but increase the fluid velocity fluctuations in the stream-wise direction. The latter arises due to the magnitude of the slip velocity between the fluid and particles in this direction in the near-wall region: particles are slightly faster than the fluid in this region and therefore may increase the local fluid momentum and thus the fluctuation in velocity. In all of the particle-laden cases, the peak of the RMS velocities shifts slightly to the centre of the channel when particles are added to the flow. The results are in general agreement with the observations reported in [2].

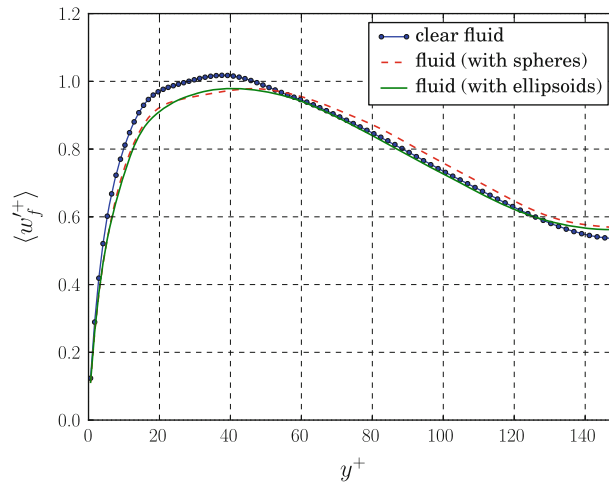


Fig. 11 Fluid span-wise direction RMS velocities as functions of the distance to the wall for: single phase (*solid line with circle*), fluid with spherical particles (*dashed line*), fluid with ellipsoidal particles (*solid line*)

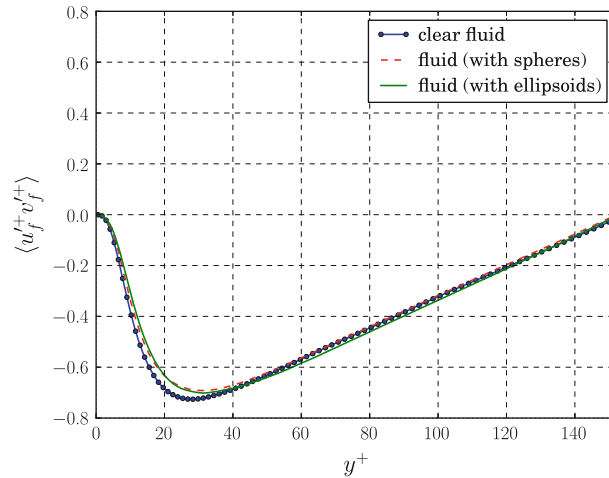


Fig. 12 Fluid Reynolds stresses as functions of the distance to the wall for: single phase (*solid line with circle*), spherical case (*dashed line*), ellipsoidal case (*solid line*)

Figure 12 shows the Reynolds stresses as functions of the distance to the wall. This Figure shows there is very little effect of the particles on the Reynolds stresses; possibly, a small shift of the curve to the centre of the channel as the particles are added.

4.2.4 Particle velocity statistics

Figure 13 shows the mean particle velocity as a function of the distance to the wall for the case considering spheres and ellipsoids. There is a small difference between the average particle velocity, comparing the spheres with the ellipsoids. This is because the higher mass loading of the ellipsoids, leading to slightly lower fluid velocities. The slip velocity is similar in both cases.

The slip velocity between the fluid and the particles in the stream-wise direction for the 2 particle-laden cases is shown in Fig. 14. It can be observed that the particles obtain their momentum from the fluid in the outer region of the boundary and the centre of the channel, for $y^+ > 20$. In the inner layer of the boundary layer, the particles add momentum to the fluid, as the slip velocity is negative. The peak of the momentum transfer lies slightly away from the wall. For the spherical particles, the momentum transfer peaks around $y^+ = 5.5$, and for the case laden with ellipsoids, the maximum in momentum transfer lies at $y^+ = 9.5$. Moreover, from the Figure, it can be seen that the ellipsoidal particles require more momentum than the spherical particles, and this is due to their higher mass loading of the ellipsoidal particles or the orientation of the ellipsoids, or a

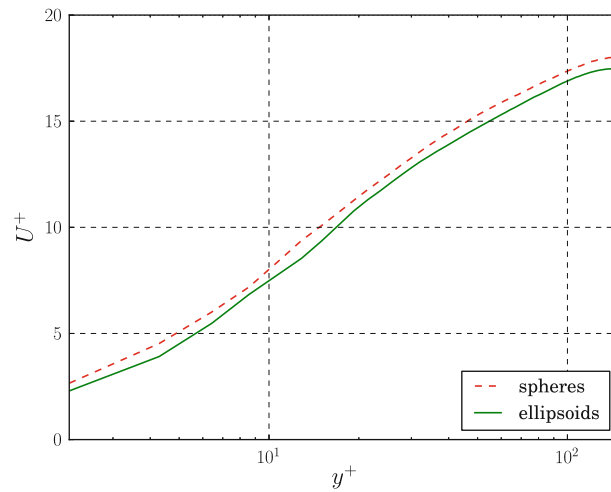


Fig. 13 Particle stream-wise direction mean velocities single phase (solid line with circle), spherical case (dashed line), ellipsoidal case (solid line)

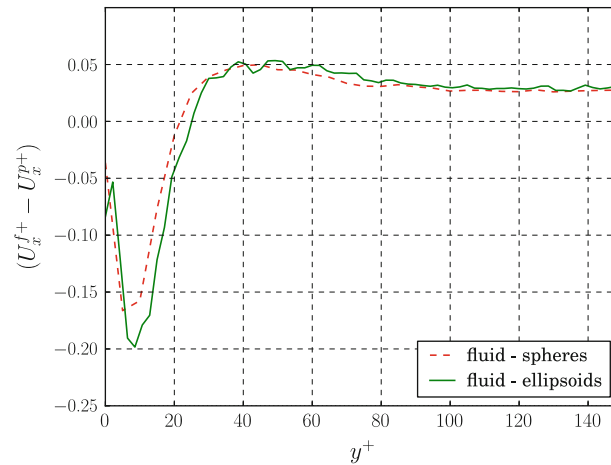


Fig. 14 The slip velocity between particles and fluid in the stream-wise direction for: spherical case (dashed line) and ellipsoidal case (solid line)

combination of the two effects. Fig. 15 shows the slip velocity between the particles and the fluid in the wall-normal direction. As the slip velocity directly drives the momentum transfer between the phases, it represents how much of the momentum of the particles is conveyed to the wall region. This means that particles quickly migrate from the centre of the channel to the wall layer and then slowly move back. As can be clearly observed, the particles are moving to the wall and are “dragging” the fluid along. Although the mass flux of particles moving towards the wall and away from the wall is the same, as the statistics predicted by the simulation have reached steady-state, particles moving towards the wall have a much higher momentum than particles moving away from the wall. This confirms that mechanism of particles obtaining momentum in the centre of the channel and transporting this momentum towards the wall even in a stationary situation. Figure 16 shows the slip velocity between the particles and the fluid in the span-wise direction. There is no momentum transfer in this direction, confirming the simulation has reached steady-state statistics prior to sampling the statistics. It should be noted that the average fluid velocity in the wall-normal and span-wise directions are zero, as the simulations have reached steady-state. Figures 17, 18 and 19 present the RMS of particle velocities and compare these to the fluid RMS velocity of the clear channel, in the stream-wise, wall-normal, and span-wise directions, respectively. The figures show that the particles have a larger RMS velocity than the fluid in the stream-wise direction, but that their RMS velocities in the other 2 directions are lower than the fluid phase. The increased RMS velocity in the stream-wise direction can be explained from the fact that there is a large mean fluid velocity gradient and a large slip velocity in the stream-wise direction. The RMS of the particle velocity

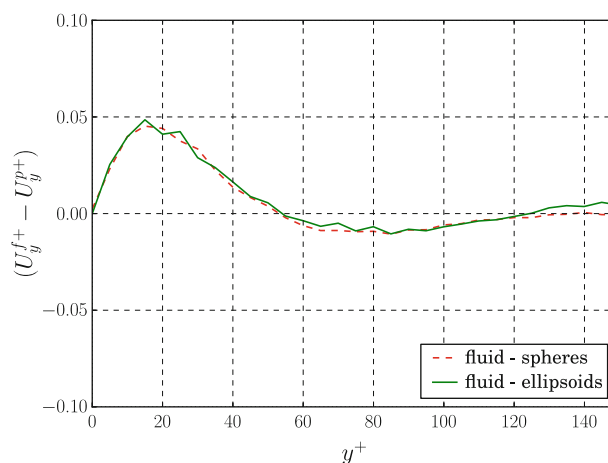


Fig. 15 Slip velocity between the particles and fluid in the wall-normal direction for: spherical case (*dashed line*) and ellipsoidal case (*solid line*)

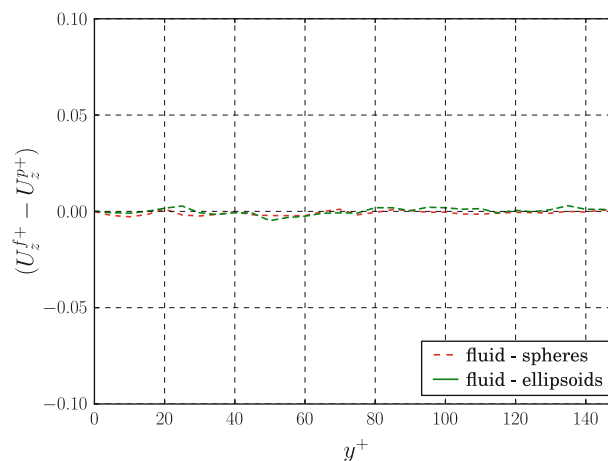


Fig. 16 Slip velocity between the particles and fluid in the span-wise direction for: spherical case (*dashed line*) and ellipsoidal case (*solid line*)

are coupled to the fluid drag, which in turn is coupled to the slip velocity between the phases. The large mean fluid velocity, the large fluid RMS velocity as well as a strong drag between the phases will enhance the RMS of the particle velocities.

On the other hand, velocity gradients and slip velocities are close to zero in span-wise and wall-normal directions and so there is almost no mean fluid drag in these two directions. Moreover, the particles have a larger response time than the fluid. Therefore, the RMS velocities of the particles are lower than those of the fluid in those directions.

The Reynolds stresses as functions of wall distance for the fluid as well as for the two particles are shown in Fig. 20. This figure shows that the Reynolds stresses of the particles are lower between $15 < y^+ < 70$, but are the same in the inner boundary layer and towards the centre of the channel.

4.2.5 Turbulence kinetic energy

In Sect. 2.5 the equation of turbulence kinetic energy (TKE) for fully developed channel flow has been given. In Eq. (46), three “transport terms” do not produce or dissipate net energy; their average over the channel is zero. These terms merely transport kinetic energy from one part in the channel to another part.

Figures 21 and 23 show the production term as well as the sum of the dissipation terms of the TKE equation, as discussed in Sect. 2.5, for the case of the clear fluid, the case with spherical particles, and the case including ellipsoidal particles. Although the differences are not large, due to the low mass loading of the

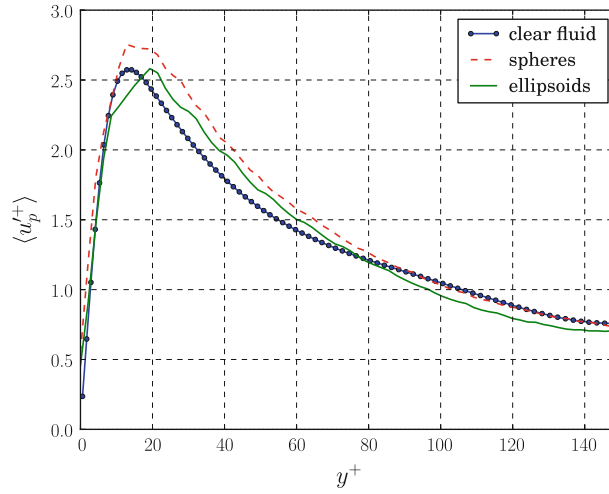


Fig. 17 The stream-wise RMS of velocities for the: clear fluid (*solid line with circle*), spherical particles (*dashed line*), ellipsoidal particles (*solid line*)

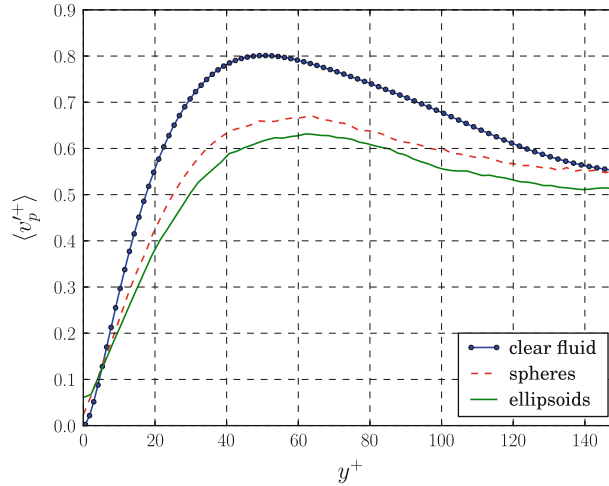


Fig. 18 The wall-normal RMS velocities for the: clear fluid (*solid line with circle*), spherical particles (*dashed line*), ellipsoidal particles (*solid line*)

particles, there are clear differences between these terms in the case without particles compared to the case with particles. Compared to the results from the clear channel, the total TKE decreases 6.0 and 4.8 % for the channel flow including spheres and ellipsoids, respectively. The particle dissipation rates are shown in Fig. 24 for the channel with spheres and ellipsoids. The dissipation caused by the spherical particles peaks around a distance of $y^+ = 6$ from the wall, whereas the peak of the dissipation caused by the presence of the ellipsoids lies around a distance of $y^+ = 8.6$ from the wall. This shift is due to the shape difference of the ellipsoids compared to the spheres. The dissipation of the ellipsoids is also more significant than that of the spheres, which is most likely an effect of the difference in mass loading. Figures 22, 25, and 26 show the effect of the particles and ellipsoids on the transport terms in the TKE equation. At the current particle concentrations, there does not seem to be an effect of the particles or ellipsoids on the transport terms on the TKE equation.

4.3 Velocity correlations

Figure 27 shows the stream-wise velocity correlation coefficient between the particles and the fluid as a function of the distance to the wall. The correlation is very high and almost constant in most of the channel, except in the region very near the wall, $y^+ < 9$. The correlation drops off significantly for the case laden with spherical

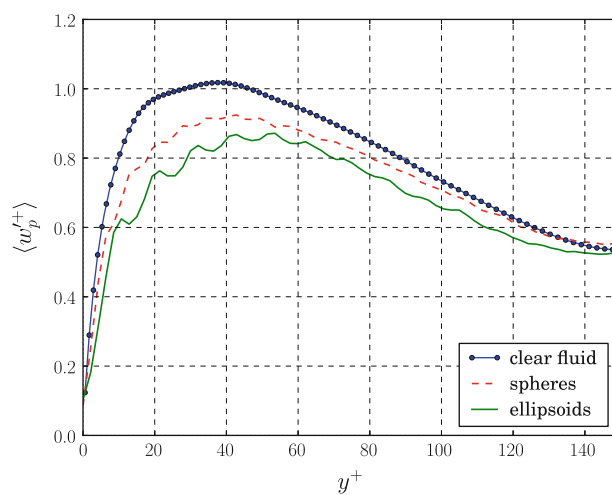


Fig. 19 The span-wise RMS of velocities for the: clear fluid (*solid line with circle*), spherical particles (*dashed line*), ellipsoidal particles (*solid line*)

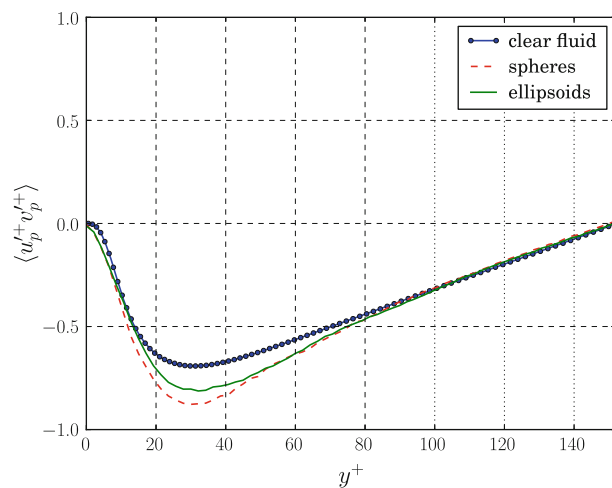


Fig. 20 Particle span-wise direction velocity RMS single phase (*solid line with circle*), spherical case (*dashed line*), ellipsoidal case (*solid line*)

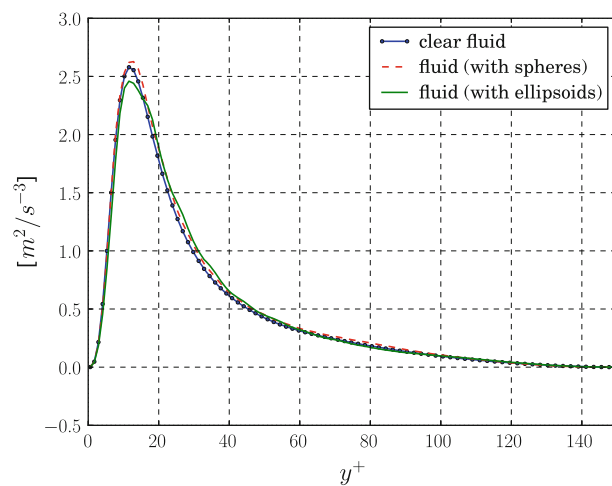


Fig. 21 The production term on the turbulence kinetic energy equation as identified in Sect. 2.5, for single phase and particle-laden cases, as a function of the distance to the wall

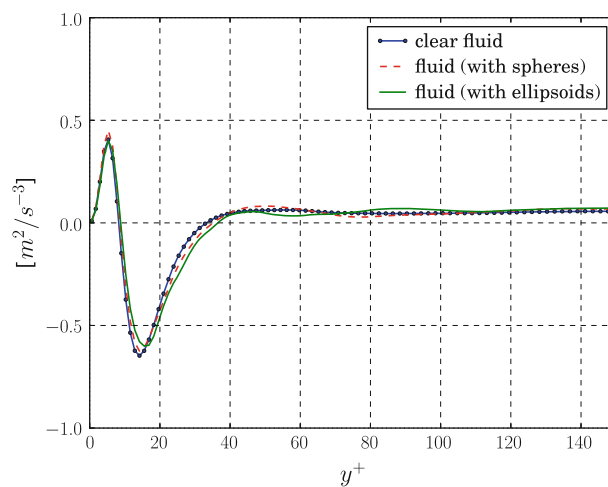


Fig. 22 The turbulence transport term on the turbulence kinetic energy equation as identified in Sect. 2.5, for particle-laden cases, as a function of the distance to the wall

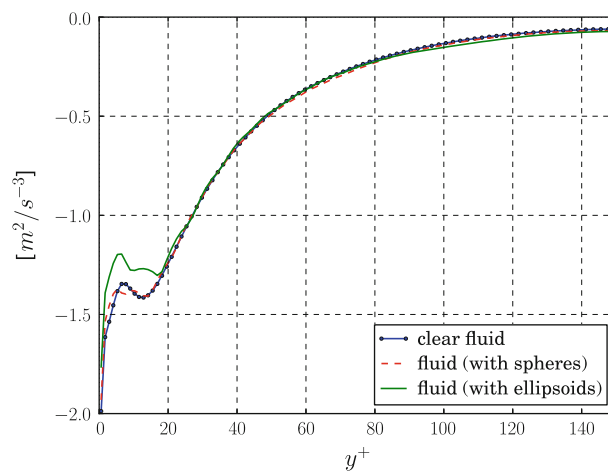


Fig. 23 The dissipation term on the turbulence kinetic energy equation as identified in Sect. 2.5, for single phase and particle-laden cases, as a function of the distance of the wall

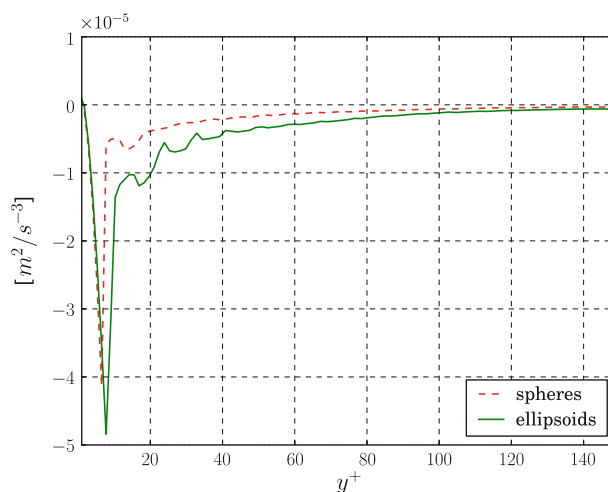


Fig. 24 Particle dissipation rate as a function of distance to the wall for: channel laden with spheres (*dashed line*), ellipsoids (*solid line*)

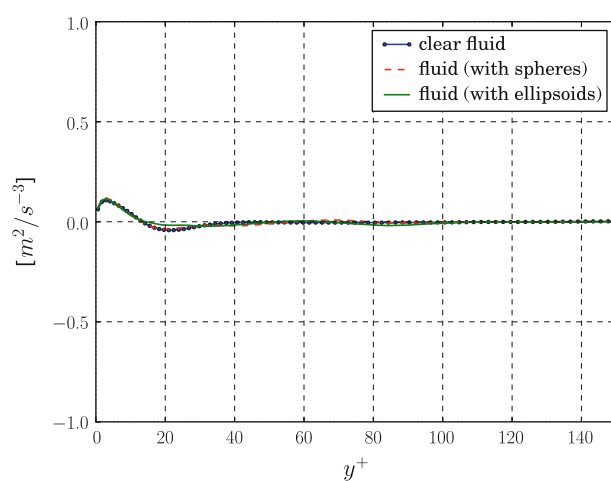


Fig. 25 The pressure transport term on the turbulent kinetic energy equation as identified in Sect. 2.5, for particle-laden cases, as a function of the distance to the wall

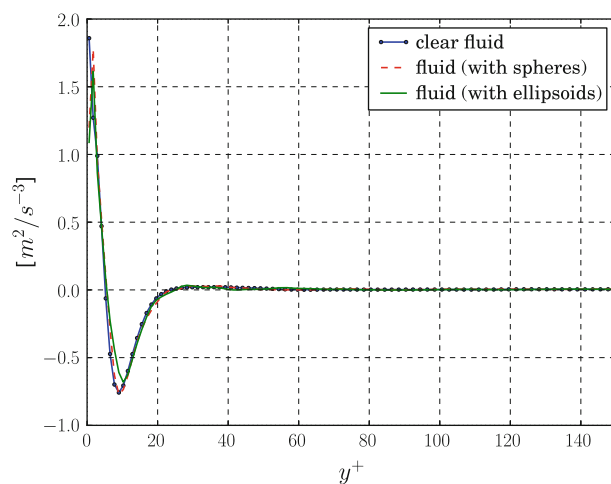


Fig. 26 The viscous transport term on the turbulence kinetic energy equation as identified in Sect. 2.5, for particle-laden cases, as a function of the distance to the wall

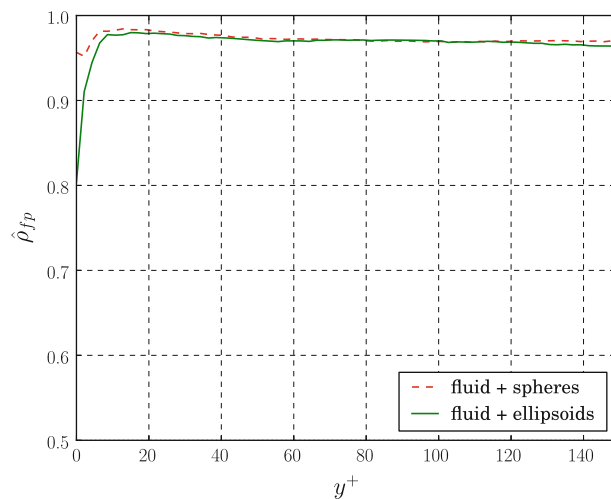


Fig. 27 The stream-wise velocity correlation coefficient between the particles and the fluid as a function of the distance to the wall

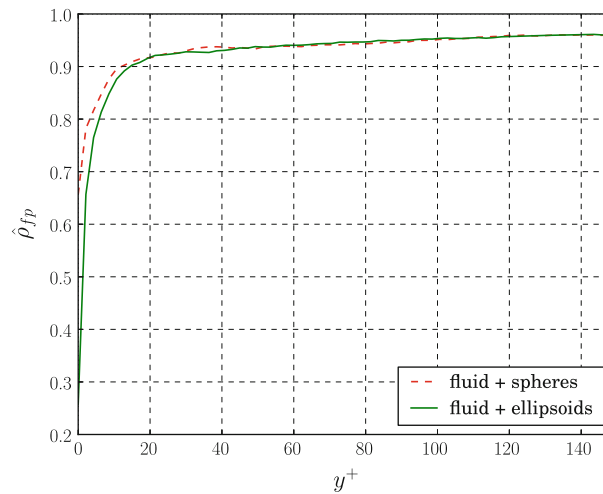


Fig. 28 The wall-normal velocity correlation coefficient between the particles and the fluid as a function of the distance to the wall

particles, but even much more so for the case concerning the ellipsoidal particles. This originates from the complex nature of the collisions between the ellipsoidal particles and the wall, involving rotation of the particle as well as some translation. For the spherical particles, the wall has most effect on the translational velocity of the particle.

Figure 28 shows the wall-normal velocity correlation coefficient between the particles and the fluid as a function of distance to the wall. The trends in this figure are similar compared to the stream-wise velocity correlation, but are even more pronounced. In near-wall region, the translational velocity of the particles in wall-normal direction strongly depends on the wall collisions. Spheres are vertically reflected by a wall collision and returned towards the centre of the channel. However, the elongated shape of the ellipsoids strongly influences the dynamics of the collisions, as it depends on the orientation of the ellipsoids when they collide with the wall. Moreover, a significant exchange of momentum between translational and rotational components can occur when the ellipsoids collide, which is not the case with spherical particles. The increased complexity of the dynamics of the collision for ellipsoids decreases the correlation of velocity in the wall-normal direction.

4.4 Orientation of ellipsoids

For spherical particles, the orientation does not change the hydrodynamic forces. However, for the ellipsoidal particles, there is a strong effect of their orientation on the hydrodynamic forces: the ellipsoid can minimise the drag by aligning the longest axis of the particle with the flow direction, or maximise the drag by aligning one of the shorter axes with the flow direction. The statistics of the results are presented in terms of the cosine value of the 3 angles between the major axes of the ellipsoid and the world space axes, as is shown in Fig. 29, where the world x axis is the direction of the average flow.

The orientation of the ellipsoids is compared to the work of [21]. In their work, the collisions between ellipsoids are neglected and collisions between the ellipsoids and the wall are not resolved, but the ellipsoidal particles are treated as elastic points when their centre comes into contact with the wall: the wall-normal velocity is reversed.

Figure 30 shows the absolute cosine value of the angle between the ellipsoid's major axis and the x axis of the world space co-ordinate as a function of distance to the wall. The X axis corresponds to the stream-wise direction of the flow. Therefore, the figure shows that the ellipsoids in the centre of the channel have almost no preferential orientation, as an average cosine value of 0.5 corresponds to a random distribution. However, the orientation of the ellipsoids becomes preferential in the flow direction near the wall, peaking around an angle of 45° at the distance from the wall of around $y^+ = 15$. Although the trends between the current simulation results are comparable to the findings of [21], there are some differences. The peak value of the angle at 45° in the current work occurs further inward the channel compared to [21]. This is attributed to a more realistic model to describe the interaction of the ellipsoids with the wall. In the current approach, the collision between a rotating ellipsoid and the wall moves the ellipsoid further into the domain than in the ad hoc particle-wall

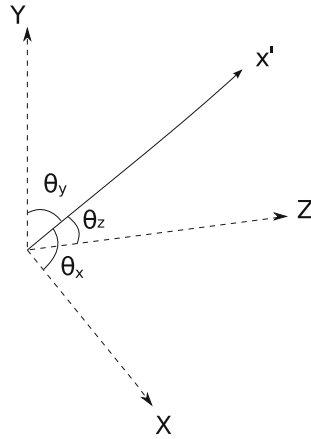


Fig. 29 The definition of the angles between the major axis of the ellipsoid, x' , and the world space axis. The mean flow is in the x direction

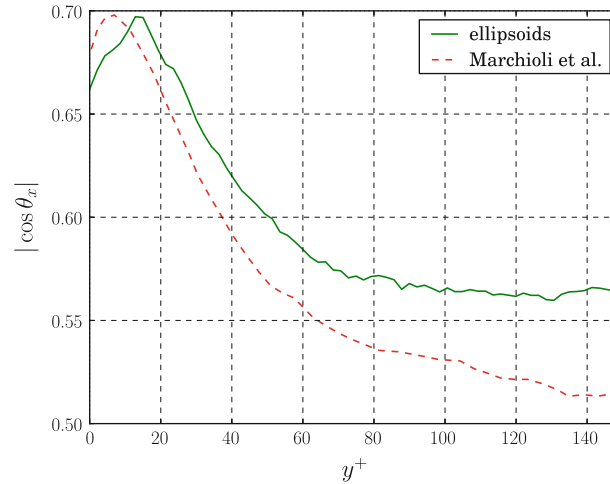


Fig. 30 The absolute cosine value of the angle between the ellipsoid's major axis and the X axis of the world space co-ordinate as a function of the distance to the wall

collision model of [21]. Moreover, there seems to be a minor effect of ellipsoid–ellipsoid collision inside the channel, as the average angle is slightly larger in the results reported in this paper.

The average absolute cosine values of the angle between the ellipsoid's major axis and the y and z axis or world space as a function of distance to the wall are shown in Figs. 31 and 32, respectively. The effect of the wall is more pronounced than the findings of [21] show, but the values inside the channel are similar and show no preferential orientation, which is expected in the case of stationary statistics. Near the wall, two effects can be observed. The first is the presence of strong fluid velocity gradients, inducing a preferential orientation of the ellipsoid through the hydrodynamic torque coupling. The second effect concerns the collisions of the ellipsoids with the wall. These collisions induce rotation on the ellipsoids and may force the ellipsoids in a specific orientation. This can be seen clearly in Fig. 32, where very close to the wall only ellipsoids are encountered which have a very large angle of orientation. This is because any other orientation would make it very difficult for the ellipsoid to be so near to the wall.

Figure 33 shows the average angular velocity of the ellipsoids as function of distance to the wall, showing both walls. As can be clearly seen, the wall and the boundary layer induce a strong angular velocity in the span-wise direction of the ellipsoids. This angular velocity leads to the orientation of the ellipsoids as observed in Figs. 30, 31 and 32. Figure 34 shows the RMS of the angular velocities of the ellipsoids as function of the distance to the wall upto the centre of the channel.

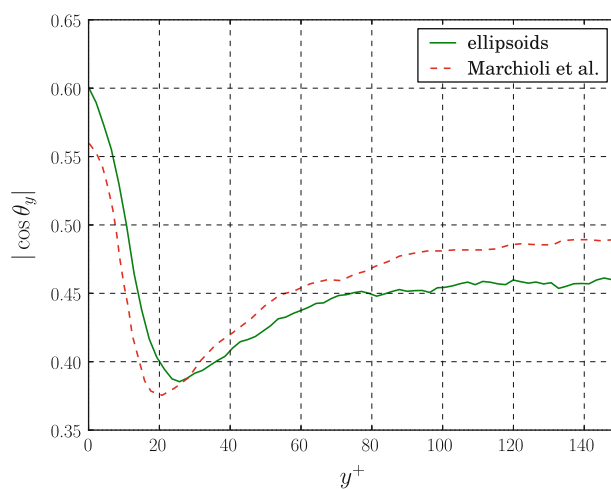


Fig. 31 The absolute cosine value of the angle between the ellipsoid's major axis and the Y axis of the world space co-ordinate as a function of the distance to the wall

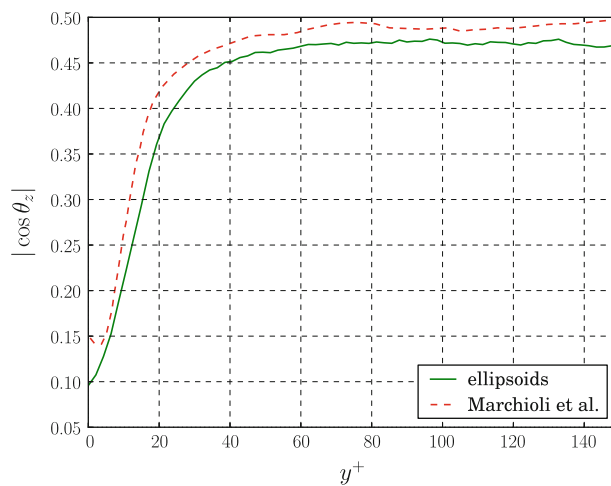


Fig. 32 The absolute cosine value of the angle between the ellipsoid's major axis and the Z axis of the world space co-ordinate as a function of the distance to the wall

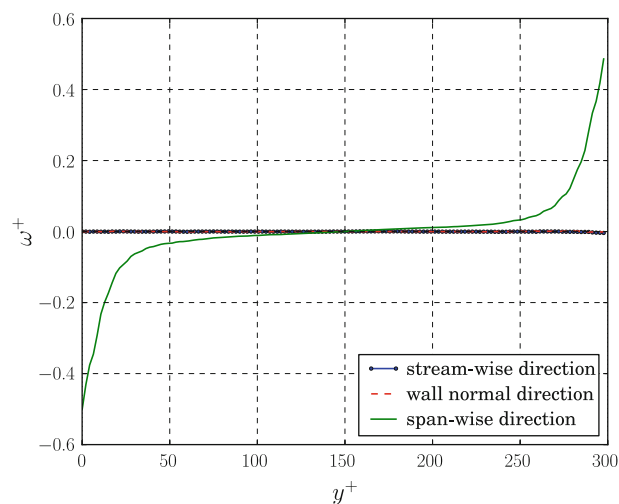


Fig. 33 The mean angular velocity of ellipsoids in the three orthogonal directions as a function of the distance to the wall, showing both walls

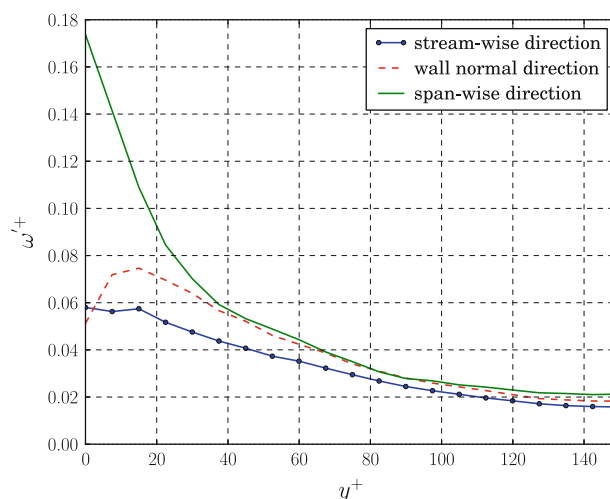


Fig. 34 The RMS of the angular velocity of the ellipsoids in the three orthogonal directions as a function of the distance to the wall

5 Conclusions

In this paper, the behaviour of very small ellipsoidal particles suspended in turbulent channel flow is elucidated using direct numerical simulation combined with the “point-source” approach and the Lagrangian tracking of the individual ellipsoids. The simulations are carried out with four-way coupling: the fluid affects the particles, the particles affect the fluid, and the particles collide with each other and the wall, by application of a newly proposed deterministic collision algorithm. A novel Quaternion framework is put forward, using an accurate time integration and avoiding the usage of a rotation matrix all together.

An analysis of the terms of the turbulence kinetic energy (TKE) equation of the fluid shows that the homogeneous dissipation of TKE caused by the fluid decreases by the addition of particles. This is because of the existence of an additional mechanism responsible for dissipation at the small scales, i.e. the dissipation resulting from the behaviour of the particles. This dissipation is caused by the slip velocity between the particles and the fluid. Almost all dissipation of TKE caused by the particles is in a thin layer in the near-wall region.

The results of the slip velocity between the fluid and the particles show that particles approach the wall with a larger momentum than they have returning to the centre of the channel. This leads to an increase of concentration of particles near the wall by a factor 4 compared to the centre of the channel. The maximum of the RMS of the fluid velocities is shifted inwards by addition of particles or ellipsoids. For the spherical particles, the RMS of particle velocities in the stream-wise direction is larger than the RMS of fluid velocity, because of the relatively large slip velocity between the phases in this direction. The RMS of the particle velocity in the other two directions is less than the RMS of the fluid velocity in the corresponding directions, because the slip velocity between the two phases is very small.

The results of orientation and angular velocity of the ellipsoidal particles show that there is no strong preferential orientation of the particles in the centre of the channel, but that the particles are aligned with the stream-wise direction in the near-wall region. This is caused by the dynamics of the boundary layer, as was previously suggested in [21], but also by the effect of particle–wall collisions. Finally, the paper shows that particle–particle and particle–wall collisions have some effect on the behaviour of the ellipsoids, even in the very dilute flow of interest in this paper.

Acknowledgments The authors are grateful to the European Cooperation in Science and Technology (COST) Action FP 1005 on “Fibre suspension flow modelling” for the fruitful meetings and discussions. We are also grateful to Dr C. Marchioli for the fruitful discussions and access to his simulation database. We would like to thank Alireza Dastan for the fruitful discussions on the hydrodynamic force models.

References

1. Allen, M.P., Tildesley, D.J.: The Computer Simulation of Liquids, vol. 42. Oxford University Press (1989). <http://link.aip.org/link/PHTOAD/v42/i3/p105/s1&Agg=doi>

2. Andersson, H.I., Zhao, L., Barri, M.: Torque-coupling and particle-turbulence interactions. *J. Fluid Mech.* **696**, 319–329 (2012). doi:[10.1017/jfm.2012.44](https://doi.org/10.1017/jfm.2012.44). http://www.journals.cambridge.org/abstract_S0022112012000444
3. Betsch, P., Siebert, R.: Rigid body dynamics in terms of quaternions: Hamiltonian formulation and conserving numerical integration. *Int. J. Numer. Methods Eng.* **79**, 444–473 (2009). doi:[10.1002/nme.2586/abstract](https://doi.org/10.1002/nme.2586/abstract)
4. Brenner, H.: The Stokes resistance of an arbitrary particle. *Chem. Eng. Sci.* **18**, 1–25 (1963). <http://www.sciencedirect.com/science/article/pii/0009250963800019>
5. Brenner, H.: The Stokes resistance of an arbitrary particle-IV arbitrary fields of flow. *Chem. Eng. Sci.* **19**, 703–727 (1964)
6. Brenner, H.: The Stokes resistance of an arbitrary particleIII: shear fields. *Chem. Eng. Sci.* **19**, 631–651 (1964). doi:[10.1016/0009-2509\(64\)85052-1](https://doi.org/10.1016/0009-2509(64)85052-1). <http://linkinghub.elsevier.com/retrieve/pii/0009250964850521>
7. Bruchmüller, J., Gu, S., Luo, K.H., van Wachem, B.: Discrete element method for multiscale modeling. *J. Multi-scale Model.* **02**(01n02), 147 (2010). doi:[10.1142/S1756973710000254](https://doi.org/10.1142/S1756973710000254). <http://www.worldscinet.com/jmm/02/0201n02/S1756973710000254.html>
8. Crowe, C.T., Sharma, M.P., Stock, D.E.: The particle-source-in cell (PSI-CELL) model for gas-droplet flows. *J. Fluids Eng.* **99**, 325–333 (1977)
9. Eaton, J.K.: Two-way coupled turbulence simulations of gas-particle flows using point-particle tracking. *Int. J. Multiph. Flow* **35**, 792–800 (2009)
10. Elghobashi, S., Truesdell, G.C.: Direct simulation of particle dispersion in a decaying isotropic turbulence. *J. Fluid Mech.* **242**, 655–700 (1992)
11. Evans, D., Murad, S.: Singularity free algorithm for molecular dynamics simulation of rigid polyatomics. *Mol. Phys.* **34**, 327–331 (1977). <http://www.tandfonline.com/doi/abs/10.1080/00268977700101761>
12. Fan, F.G., Ahmadi, G.: A sublayer model for turbulent deposition of particles in vertical ducts with smooth and rough surfaces. *J. Aerosol Sci.* **24**, 45–64 (1993). <http://www.sciencedirect.com/science/article/pii/002185029390084M>
13. Fan, F.G., Ahmadi, G.: A sublayer model for wall deposition of ellipsoidal particles in turbulent streams. *J. Aerosol Sci.* **26**, 813–840 (1995). doi:[10.1016/0021-8502\(95\)00021-4](https://doi.org/10.1016/0021-8502(95)00021-4). <http://linkinghub.elsevier.com/retrieve/pii/0021850295000214>
14. Fan, F.G., Ahmadi, G.: Wall deposition of small ellipsoids from turbulent air flows-a Brownian dynamics simulation. *J. Aerosol Sci.* **31**, 1205–1229 (2000). doi:[10.1016/S0021-8502\(00\)00018-5](https://doi.org/10.1016/S0021-8502(00)00018-5). <http://linkinghub.elsevier.com/retrieve/pii/S0021850200000185>
15. Gallily, I., Cohen, A.: On the orderly nature of the motion of nonspherical aerosol particles. II. Inertial collision between a spherical large droplet and an axially symmetrical elongated particle. *J. Colloid Interface Sci.* **68**, 338–356 (1979). <http://www.sciencedirect.com/science/article/pii/0021979779902868>, <http://www.sciencedirect.com/science/article/pii/002197977990287X>
16. Gillissen, J., Boersma, B.J., Mortensen, P., Andersson, H.: Fibre-induced drag reduction. *J. Fluid Mech.* **602**, 209–218 (2008). doi:[10.1017/S0022112008000967](https://doi.org/10.1017/S0022112008000967)
17. Jeffery, G.B.: The motion of ellipsoidal particles immersed in a viscous fluid. *Proc. R. Soc. Lond. Ser. A, Containing Papers of a Mathematical and Physical Character* **102**, 161–179 (1922). <http://www.jstor.org/stable/94111>
18. Kulick, J., Fessler, J., Eaton, J.: Particle response and turbulence modification in fully developed channel flow. *J. Fluid Mech.* **277**, 109–134 (1994). http://journals.cambridge.org/abstract_S0022112094002703
19. Kussin, J., Sommerfeld, M.: Experimental studies on particle behaviour and turbulence modification in horizontal channel flow with different wall roughness. *Exp. Fluids* **33**, 143–159 (2002). doi:[10.1007/s00348-002-0485-9](https://doi.org/10.1007/s00348-002-0485-9). <http://www.springerlink.com/index/4DD9HQYBAK30R4YG.pdf>
20. Lain, S., Sommerfeld, M., Kussin, J.: Experimental studies and modelling of four-way coupling in particle-laden horizontal channel flow. *Int. J. Heat Fluid Flow* **23**, 647–656 (2002)
21. Marchioli, C., Fantoni, M., Soldati, A.: Orientation, distribution, and deposition of elongated, inertial fibers in turbulent channel flow. *Phys. Fluids* **22**, 033,301 (2010). doi:[10.1063/1.3328874](https://doi.org/10.1063/1.3328874). <http://link.aip.org/link/PHFLE6/v22/i3/p033301/s1&Agg=doi>
22. Marchioli, C., Soldati, A., Kuerten, J.G.M., Arcen, B., Taniere, A., Goldensoph, G., Squires, K.D., Cargnelutti, M.F., Portela, L.M.: Statistics of particle dispersion in direct numerical simulations of wall-bounded turbulence: results of an international collaborative benchmark test. *Int. J. Multiph. Flow* **34**, 879–893 (2008). doi:[10.1016/j.ijmultiphaseflow.2008.01.009](https://doi.org/10.1016/j.ijmultiphaseflow.2008.01.009). <http://www.sciencedirect.com/science/article/pii/S0301932208000414>
23. Maxey, M.R., Riley, J.J.: Equation of motion for a small rigid sphere in a nonuniform flow. *Phys. Fluids* **26**, 883 (1983). doi:[10.1063/1.864230](https://doi.org/10.1063/1.864230). <http://link.aip.org/link/PFLDAS/v26/i4/p883/s1&Agg=doi>
24. McLaughlin, J.B.: Aerosol particle deposition in numerically simulated channel flow. *Phys. Fluids A: Fluid Dyn.* **1**, 1211 (1989). doi:[10.1063/1.857344](https://doi.org/10.1063/1.857344). <http://link.aip.org/link/PFADEB/v1/i7/p1211/s1&Agg=doi>
25. Mindlin, R.D., Deresiewicz, H.: Elastic spheres in contact under varying oblique forces. *J. Appl. Mech.* **20**, 327–344 (1953). <http://www.citeulike.org/group/13900/article/7798914>
26. Mortensen, P., Andersson, H., Gillissen, J., Boersma, B.: On the orientation of ellipsoidal particles in a turbulent shear flow. *Int. J. Multiph. Flow* **34**, 678–683 (2008). doi:[10.1016/j.ijmultiphaseflow.2007.12.007](https://doi.org/10.1016/j.ijmultiphaseflow.2007.12.007). <http://linkinghub.elsevier.com/retrieve/pii/S0301932208000098>
27. Mortensen, P., Andersson, H., Gillissen, J., Boersma, B.J.: Dynamics of prolate ellipsoidal particles in a turbulent channel flow. *Phys. Fluids* **20**, 093,302 (2008). doi:[10.1063/1.2975209](https://doi.org/10.1063/1.2975209). <http://link.aip.org/link/PHFLE6/v20/i9/p093302/s1&Agg=doi>
28. Mortensen, P.H., Andersson, H.I., Gillissen, J., Boersma, B.J.: Particle spin in a turbulent shear flow. *Phys. Fluids* **19**, 078,109 (2007). doi:[10.1063/1.2750677](https://doi.org/10.1063/1.2750677). <http://link.aip.org/link/PHFLE6/v19/i7/p078109/s1&Agg=doi>
29. Shapiro, M., Goldenberg, M.: Deposition of glass fiber particles from turbulent air flow in a pipe. *J. Aerosol Sci.* **24**, 65–87 (1993). <http://www.sciencedirect.com/science/article/pii/002185029390085N>
30. Snyder, W., Lumley, J.: Some measurements of particle velocity autocorrelation functions in a turbulent flow. *J. Fluid Mech.* **48**, 41–71 (1971)

31. Squires, K.D., Eaton, J.K.: Preferential concentration of particles by turbulence. *Phys. Fluids A: Fluid Dyn.* **3**, 1169 (1991). doi:[10.1063/1.858045](https://doi.org/10.1063/1.858045). <http://link.aip.org/link/PFADEB/v3/i5/p1169/s1&Agg=doi>
32. Tian, L., Ahmadi, G.: Particle deposition in turbulent duct flows comparisons of different model predictions. *J. Aerosol Sci.* **38**, 377–397 (2007). doi:[10.1016/j.jaerosci.2006.12.003](https://doi.org/10.1016/j.jaerosci.2006.12.003). <http://linkinghub.elsevier.com/retrieve/pii/S002185020700002X>
33. van Wachem, B., Zastawny, M., Mallouppas, G., Zhao, F., Denner, F., Pennefather, J.C.: <http://www.multiflow.org/> (2012)
34. Walton, O.R.: Numerical simulation of inclined chute flows of monodisperse, inelastic, frictional spheres. *Mech. Mater.* **16**, 239–247 (1993)
35. Walton, O.R., Braun, R.L.: Simulation of rotary-drum and repose tests for frictional spheres and rigid sphere clusters. DOE/NSF Workshop on Flow of Particulates (1993). http://www.grainflow.com/index_files/Rotary_Drum_Simulation_DOE-NSF-1993.pdf
36. Yeung, P., Pope, S.: An algorithm for tracking fluid particles in numerical simulations of homogeneous turbulence. *J. Comput. Phys.* **79**, 373–416 (1988)
37. Zhang, H., Ahmadi, G., Fan, F.G., McLaughlin, J.B.: Ellipsoidal particles transport and deposition in turbulent channel flows. *Int. J. Multiph. Flow* **27**, 971–1009 (2001). <http://www.sciencedirect.com/science/article/pii/S0301932200000641>